

Supplementary Information

Influence of crystalline defects on magnetic nano-domains in a rare-earth-free magnetocrystalline anisotropic alloy

Dhanalakshmi Palanisamy¹, András Kovács², Omkar Hegde¹, Rafal E. Dunin-Borkowski², Dierk Raabe¹, Tilmann Hickel¹, and Baptiste Gault^{1,3}

¹ Max-Planck-Institut für Eisenforschung GmbH, 40237 Düsseldorf, Germany

² Ernst Ruska-Centre for Microscopy and Spectroscopy with Electrons, Peter Grünberg Institute, Forschungszentrum Jülich, 52425 Jülich, Germany

³ Department of Materials, Royal School of Mines, Imperial College London, London, UK

S1. Experimental Methods

Mn-Al fabrication. The ferromagnetic MnAl τ -phase is prepared by conventional vacuum arc melting process. Al and Mn elements with purity $\sim 99.99\%$ in the form of shots were mixed with appropriate atomic ratio and were melted in a vacuum arc melting unit under high purity argon atmosphere (99.999%) using a water-cooled copper hearth and a tungsten electrode. The solidified ingot (30 grams) was subsequently homogenized at 1100°C for 10 hours in a muffle furnace followed by immediate water quenching to retain the high temperature hexagonal ϵ -phase at room temperature. The homogenized ingot of ϵ -phase is annealed at 450°C for 2 hours for complete phase transformation of ϵ -phase to the ferromagnetic τ -phase.

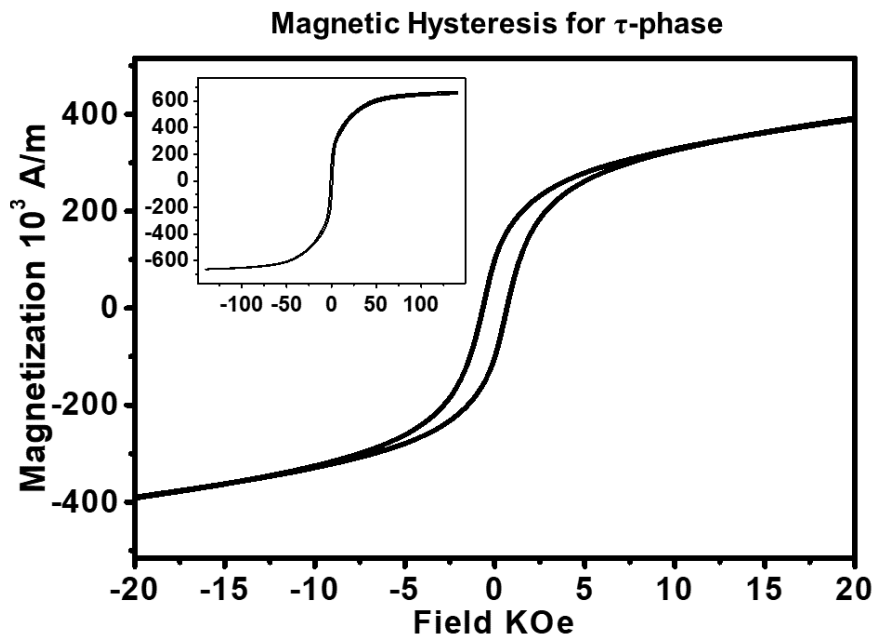


Figure S1: *Magnetic hysteresis for τ -phase*

Correlative APT/TEM sample preparation. Needle shaped specimens for correlative TEM and APT analysis were fabricated from the micro-twin regions in τ -phase sample in a dual beam scanning electron microscope (SEM)/focused-ion-beam (FIB) instrument (FEI Helios Nanolab 600i) by using an in-plane in-situ-lift-out procedure illustrated in references [20,21]. A rectangular lamella containing micro-twins was cut from the bulk τ -phase sample and was positioned and welded on the electro-polished micro-tips of a halved TEM Mo-grid using an in-situ gas injection system. This Mo-grid was held on a special correlative holder designed in-house that can be transferred from FIB to TEM directly [22]. First the mounted regions on the Mo-grid were sharpened in FIB by using Ga-ions accelerated under 30 kV with currents between 90 to 240 pA. The sharpening was carried out until the micro-twins are located within the 200 nm length from the apex of the needle specimens. Before performing TEM and APT analysis, the sharpened needles were cleaned by using a Ga-ions with low 5kV with 8pA current to remove the high energy Ga-ion induced damaged regions.

TEM lamellae from the τ -phase sample for off-axis holography experiments were also fabricated by using dual SEM/FIB instrument. The rectangular lamellae were cut from the micro-twin regions and were mounted on a TEM Cu-grid holder. The mounted lamellae were thinned up to 100 nm by using Ga-ions accelerated with 30kV and currents between 90 to 240 pA. The thinned TEM lamellae were also cleaned by 2kV and 8 pA current before performing the holography experiments.

Transmission electron microscopy (TEM). Electron diffraction analysis and High-resolution atomic scale imaging was carried out on the APT needles by using JEOL JEM-2200FS operated at 200kV and aberration-corrected Titan microscope operated at 300kV.

Atom probe tomography (APT). Compositional measurements at near-atomic scale for the needle shaped specimens were carried out using a LEAPTM 5000 XS instrument (Cameca make) operated in a laser pulsing mode with a pulse repetition rate of 200 kHz and a pulse energy of 40pJ. The specimen's base temperature was kept at 60 K and a target detection rate of ions was set to 5 ions detected per 1000 pulses. The obtained data reconstruction and analysis was performed using IVASTM 3.8.2 and 3.8.4 software.

Off-axis electron holography. The FIB prepared τ -MnAl specimens were studied in magnetic field free conditions (Lorentz mode) using an aberration-corrected transmission electron microscope (ThermoFisher Titan 60-300) operated at 300 kV. The electron holograms were generated by applying a typical 100 V on an electrostatic biprism inserted at the conjugated

image plane of the microscope. The characteristic fringe spacing was approximately 3 nm with a contrast value of ~30%. The defocused Fresnel images and electron holograms were recorded using a direct electron detecting camera (Gatan K2 IS) in counting mode [23]. The magnetic contribution to the total phase was separated from the mean inner potential by turning the specimen over inside the microscope using a custom-made on-axis tomography holder [24] (see Supplementary Information). The electron holograms were processed using a Gatan Microscopy Suite and a custom-made software package written in Semper programming language [25].

DFT calculations. First-principles density-functional theory (DFT) calculations are performed with the Vienna Ab-initio Simulation Package (VASP) [26], within the framework of the Perdew-Burke-Ernzerhof (PBE) generalized-gradient approximation (GGA) [27,28], using the projector augmented wave (PAW) [29,30] formalism. Supercells of 72 atoms are used for all calculations. Bulk supercells are oriented along [100], [010], [001] directions and twin boundary supercells are oriented along [11-2], [111], [1-10] directions. In order to understand the changes in DWEs and MAEs because of the introduction of twin boundary into the bulk, the twin boundary supercells for DWE and MAE calculations are chosen such that all the atoms are twin boundary atoms and not bulk-like. Further, we confirmed that the DWE is converged with respect to the supercell width, height and thickness, by carrying out benchmark calculations for equal stoichiometric composition with larger supercells of 144 atoms for both bulk and twin. An energy cut-off of 500 eV and a Monkhorst-Pack k -point mesh of $2 \times 5 \times 10$ is used for calculations. The energy cut-off and the k -mesh distribution are chosen after carrying out a set of calculations for the convergence of supercell energies. All calculations are performed with Methfessel-Paxton smearing [31], with a width of 0.1 eV. The convergence criterion for the total energy in electronic relaxation is 10^{-6} eV and the convergence criterion for forces in ionic relaxation is 0.01 eV/Å. All the calculations are fully volume relaxed, except while determining magneto-crystalline anisotropies (MAE), where an already relaxed structure is used for the non-self-consistent calculation. A higher electronic convergence criterion of 10^{-7} eV is used for calculating MAEs and the spin-orbital coupling is taken into account. For the bulk $L1_0$ face-centered tetragonal (fct) supercell, the converged values of equal stoichiometric lattice parameters are: $a = 3.88$ Å, $c = 3.50$ Å.

The supercell energies of body-centered cubic (bcc) Mn and face-centered cubic (fcc) Al are used as chemical potentials in determining solution enthalpies and formation energies. In the case of off-stoichiometric bulk calculations, energies are averaged over 4 different chemical

configurations. On the other hand, in the case of calculations involving off-stoichiometric twins, the energies are averaged over 6 different chemical configurations, to confirm that the low DWEs and MAEs are indeed substantially lower in each chemical configuration. The twin boundary formation energies (TBEs) are evaluated as, $TBE = (E_{twin} - E_{bulk})/2A$. Here E_{twin} is the TB supercell energy, E_{bulk} is the bulk supercell energy, and A is the area of the TB. Solution enthalpies (SEs) are calculated as, $[E^{Mn_{55.5}Al_{44.5}} - E^{Mn_{50}Al_{50}} - x(E^{Mn,chem} - E^{Al,chem})]/x$, where $E^{Mn_{55.5}Al_{44.5}}$ is the supercell energy of $Mn_{55.5}Al_{44.5}$, $E^{Mn_{50}Al_{50}}$ is the supercell energy of $Mn_{50}Al_{50}$, x is the number of atoms of Al replaced by Mn in the second sublattice of $Mn_{50}Al_{50}$ to achieve $Mn_{55.5}Al_{44.5}$ composition, $E^{Mn,chem}$ and $E^{Al,chem}$ are the chemical potentials of Mn and Al respectively. Domain wall energies (DWEs) are calculated as the difference in supercell energies with 180° DW and without DW per unit area of the domain wall. The DW width is assumed to be negligible. Magnetocrystalline anisotropy energy (MAE) is defined as the difference in the energy of supercell with magnetic moments oriented along the easy axis and the energy of supercell with magnetic moments oriented along the hard axis. For the bulk $L1_0$ structure, the easy axis is along the c-axis [001]. On the other hand, for the twin structure, the easy axis is found to be lying along the twin boundary axis [11-2].

S2. Magnetic imaging in transmission electron microscopy

We analyzed the magnetic microstructure of τ -MnAl alloys in correspondence to the structural and DFT studies. The magnetic states of the electron transparent specimen were analysed in magnetic field free conditions using Fresnel defocused imaging and off-axis electron holography. In the presence of an electric E or magnetic field B , an incident electron wave experiences the Lorentz force $\mathbf{F} = -e(\mathbf{E} + \mathbf{v}\mathbf{B})$, where e is the electron charge and \mathbf{v} is the velocity of the electron. The electron beam deflection or the electron phase change can be used to image the field variations in the sample.

Figure S2 shows the basic principles of the Fresnel imaging and off-axis electron holography. In the Fresnel method the electrons deflected by the in-plane magnetic field of the sample. Consequently, a contrast intensity maximum (or minimum) forms in the defocused image planes at the locations of the magnetic domain walls. It is difficult to extract any quantitative information from the Fresnel images other than that the presence of magnetic domains in the sample. In off-axis electron holography, the phase change in the passing electron wave due to the in-plane magnetic field in the sample is measured quantitatively.

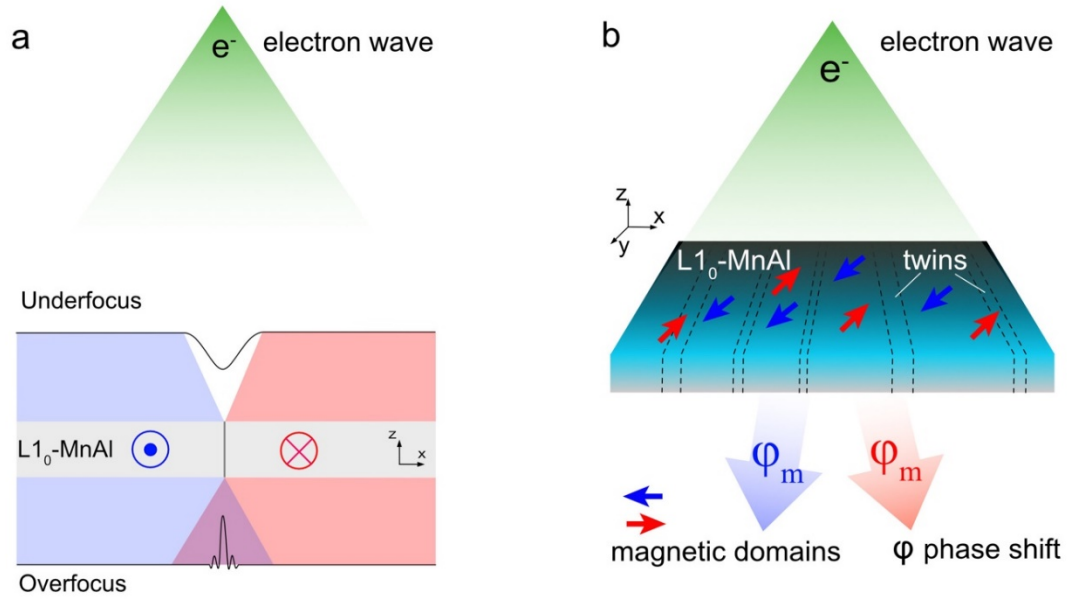


Figure S2: Simplified schematic diagrams of (a) Fresnel defocused imaging of Lorentz microscopy and (b) off-axis electron holography. For each technique, the conventional microscope objective lens is switched off in order to create a magnetic field-free environment at the position of the sample.

S3. Off-axis electron holography measurement and processing steps

An off-axis electron hologram (Figure S3a) is an interference pattern formed by the superposition of a complex specimen wave with a tilted reference wave. Its intensity distribution contains the electron wavefunction in the image plane with the amplitude and phase information. An inverse Fourier transformation method allows to recover the unwrapped total phase (Figure S2b) image that contains both the electrostatic and magnetic contributions. In the absence of long-range charge distribution, the electrostatic potential comprises primarily the mean inner potential (MIP). The magnetic phase shift scales with the in-plane magnetic vector potential in the sample. We separated the two contributing phase components by turning the specimen over inside the electron microscope. Half the sum of the two total phase images results in the MIP image of the sample that depends from the composition, density and ionicity of the sample. The vertical lines in the MIP image of τ -MnAl in Figure S1c are the small thickness variations in the specimen that was induced by the Ga ion beam sputtering. Half the difference of the total phase images gives the magnetic phase shift map (Figure S3d) expressed in *radians*. The magnetic phase image is directly proportional to the in-plane component of the magnetic induction. The visual representation of the projected in-plane magnetic field can be obtained by adding contours by evaluating the cosine of the chosen multiple of the magnetic

phase image (Figure S3e). The axial derivatives of the phase image can also be used to generate colors (Figure S3f), with the direction and magnitude of the projected in-plane magnetic induction represented by the hue and intensity of the colors, respectively.

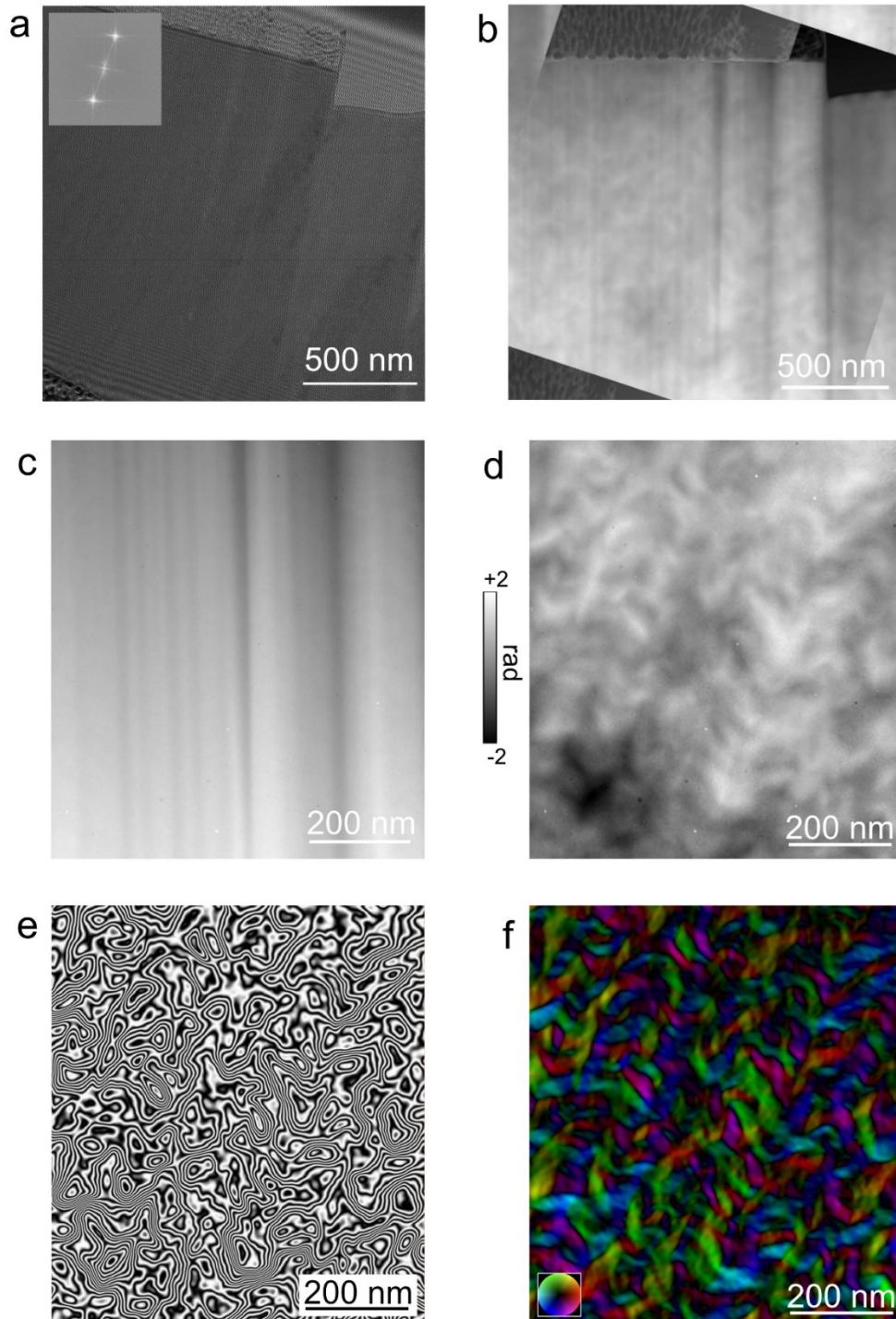


Figure S3: Magnetic induction measurement by off-axis electron holography. (a) Electron hologram. Inset is the fast Fourier transform of the hologram showing a centre band and two conjugate side-bands. (b) Unwrapped total phase image. (c) Mean inner potential map. (d) Magnetic phase shift map. (e) Contour map, the spacing is 0.15 radian. (f) Colour map.

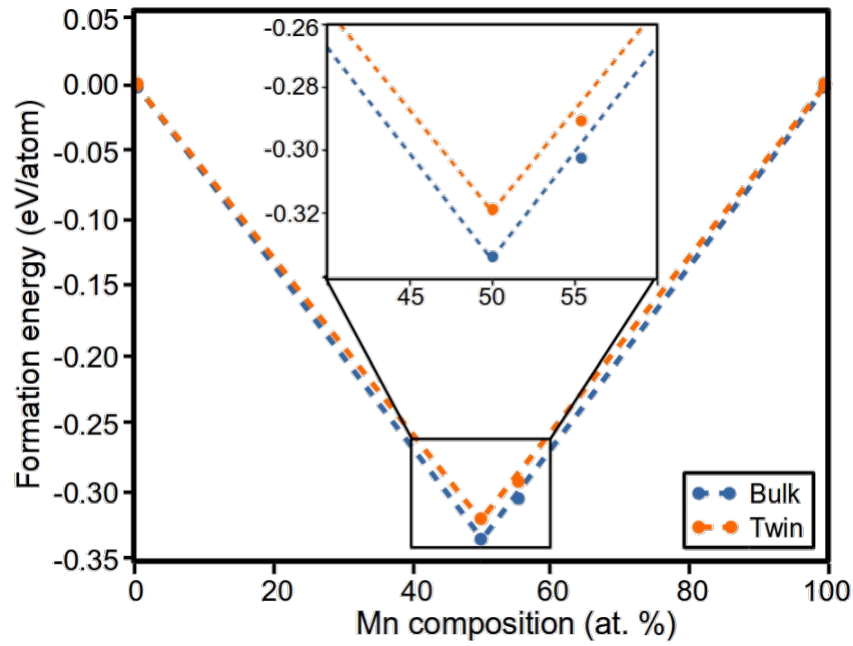


Figure S4. Convex hull connecting the formation energy of bulk and twinned $Mn_{50}Al_{50}$ and $Mn_{55.5}Al_{44.5}$ with the chemically pure end members obtained from ab-initio calculations.

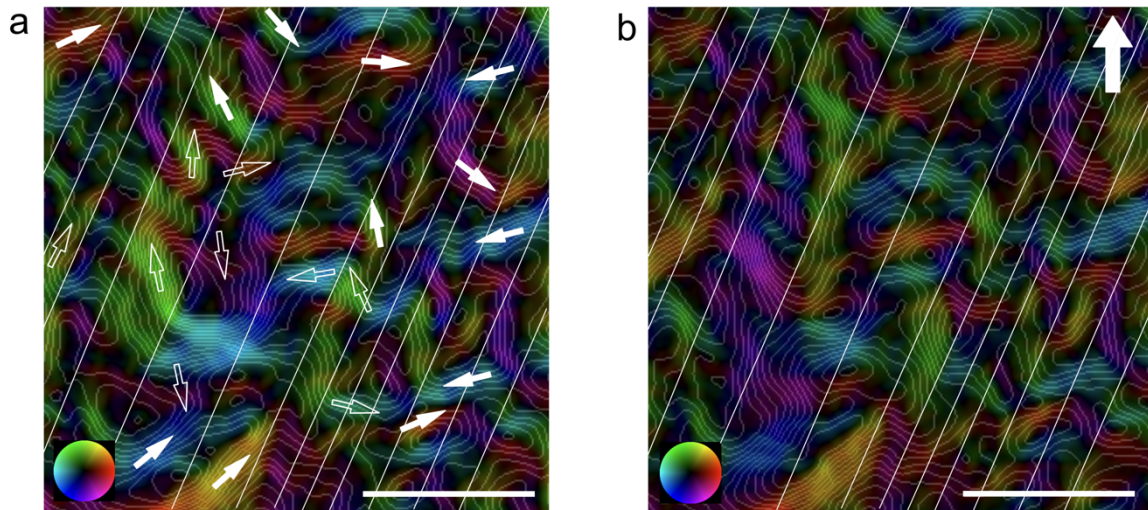


Figure S5: Magnetic induction maps recorded at the remanent state (0 mT) (a) before and (b) after magnetic saturation using a 1.41 T field. The white contrast lines mark the twin locations in the sample. (a) The empty arrows mark the domains that rearrange after the saturation, while the solid arrows mark the domains that do not change. The arrow in (b) indicates the magnetic field direction used to saturate the sample.